Laser Thomson Scattering Measurements of Electron Temperature and Density in the Near-Field Plume of a Hall-Effect Thruster

Robert L. Washeleski*, Edmond J. Meyer*, and Lyon B. King†
Michigan Technological University, Houghton, MI, 49931, USA

Non-invasive measurements of electron temperature and density in the near-field plume of a Hall-effect thruster were performed using a laser Thomson scattering diagnostic. Laser measurements were processed using a maximum likelihood estimation method and results were compared to electrostatic double probe measurements. Electron temperature ranged from approximately $1 - 40$ eV and density ranged from $1.0 \times 10^{17}\, m^{-3}$ to $1.3 \times 10^{18}\, m^{-3}$ over discharge voltages from 250 to 450 V and mass flow rates of 40 to 80 SCCM.

Nomenclature

A_p = probe area
e = fundamental charge
I = probe current
I_{Bohm} = Bohm ion current
I_R = Rayleigh intensity
I_{sat} = ion saturation current
I_T = Thomson intensity
k_B = Boltzmann's constant
m_e = electron mass
m_i = ion mass
n = particle number density
n_e = electron number density
n_i = ion number density
n_R = particle number density during Rayleigh calibration
p = gas pressure
P_R = laser power during Rayleigh calibration
P_T = laser power during Thomson scattering measurement
r_p = probe radius
T = gas temperature
T_e = electron temperature
T_i = ion temperature
$v_{i,th}$ = ion thermal speed
β = mean detector gain
$\Delta\lambda_{1/e}$ = $1/e$ half-width
λ_D = Debye length

*Graduate Research Assistant, Mechanical Engineering-Engineering Mechanics Department, 815 R. L. Smith Bldg, Student Member.
†Ron and Elaine Starr Professor of Space Systems, Mechanical Engineering-Engineering Mechanics Department, 1014 R. L. Smith Bldg, AIAA Member.

I. Introduction

Hall-effect thrusters (HETs) are compact electric space propulsion devices with long life and high specific impulse that are used on a variety of satellites for station keeping and orbit transfer manoeuvers.[1] A detailed understanding of the plasma properties in Hall-effect discharges is important for the development of the next generation of Hall thrusters and for validation of numerical plasma simulations of bounded Hall-effect discharges in general. HET technology is well developed but the plasma properties in the discharge are not completely understood, mainly due to the difficulty involved in performing accurate measurements in the near-field plume and inside the discharge channel itself. Researchers have performed probe measurements in the near-field plume and discharge channel using fast-positioning stages,[2–4] but fast-probe measurement methods have some significant disadvantages. Probes in close proximity to the thruster exit plane can significantly disrupt thruster operation, and thus alter the electron temperature and density. Another problem is that most probe data analysis techniques assume that the plasma is isotropic and Maxwellian, which may not be true due to the strong magnetic fields present near the thruster exit plane. While fast-probe studies have expanded our understanding of the temperature and density in HET discharges, a non-invasive method of measuring the electron temperature and density in the plasma is highly desirable.

Lasers have been used to measure plasma properties since shortly after they were developed in practical form in the 1960's.[5] An alternative to electrostatic probes is a non-perturbing laser diagnostic technique that measures Thomson scattering from the plasma. Thomson scattering is the process by which photons are elastically scattered from the free electrons in a plasma. Since the electrons have thermal energy their motion causes a Doppler shift in the scattered photons that is proportional to their velocity along the scattering vector, the direction of which is determined by the incident laser beam and the location of the collection optics. Like electrostatic probes, laser Thomson scattering (LTS) can be used to determine the temperature and density of free electrons in the plasma. Since Thomson scattering actually measures the electron velocity distribution function no assumptions of the plasma conditions are required, allowing accurate measurements in anisotropic and non-Maxwellian plasmas. Thomson scattering has some excellent advantages over electrostatic probes, but the scattered signal can be difficult to measure for the plasma conditions typical of Hall thrusters. Performing LTS requires a complicated measurement apparatus composed of expensive components, and establishing accurately aligned optical access to the plasma can be difficult. If these experimental difficulties can be overcome LTS has the potential to provide accurate, non-perturbing measurements of electron temperature and density that are currently unavailable to researchers in the field.

The goal of this work was to perform laser Thomson scattering measurements in the near-field plume of a Hall-effect thruster in order to assess the feasibility of LTS diagnostics on HETs. A conventional electrostatic double probe was used to perform measurements of electron temperature and density for comparison with laser measurements, and measurements with both systems were performed at a variety of thruster operating conditions. The results of the probe and laser measurements were compared in order to assess Thomson scattering measurements performed in the plume of a Hall thruster. This work is the first known application of laser Thomson scattering to a Hall-effect plasma source.

II. Experimental Equipment

The Hall-effect thruster used for this work was a 2-kW-class thruster similar to an Aerojet BPT-2000.[6–10] The outer diameter of the thruster body is 120 mm and the channel width is 13 mm. Nominal power input is 2200 W at 350 V, which yields a specific impulse of 1,765 seconds (operating on xenon) with approximately 50% efficiency. The thruster weighs 5.3 kg and was operated at a variety of flow rates using xenon as the propellant gas.

A Quantel YG980 Q-switched Nd:YAG laser with second harmonic generation was used for this work. Output energy is 610 mJ at 532 nm with a pulse duration of 6 ns (full width at half-maximum). The laser has excellent operational stability, with shot-to-shot power drift of less than 4% over 8 hours of operation and pointing stability of $< 0.45\ \mu$rad. A 1-inch-diameter plano-convex lens focuses the beam into plasma, with the focal point located on the discharge channel center-line 10 mm downstream from the thruster exit plane. After passing through the plume the beam was dissipated in a custom beam dump.

Two lenses in infinite-conjugate configuration were used to collect and focus the scattered light onto the spectrograph entrance slit. The first lens collects and collimates the scattered light from the plasma. In order to maximize the signal passed to the detector the lens must collect as much light as possible. A

76.2-mm-diameter lens with a focal length of 100 mm was chosen for the collimating lens, which gives an extremely fast f/# of 1.3. The second lens has a focal length of 300 mm in order to match the spectrograph input solid angle. The difference in focal lengths leads to a magnification of the image of the scattering volume by a factor of 2.97

The spectrograph used for this work was a Spex® Triplemate 1877C-AG triple spectrograph. This imaging spectrograph is designed to provide excellent spectral resolution combined with a flat focal plane for use with two-dimensional imaging devices. The first stage consists of two Czerny-Turner monochromators with 600 gr/mm gratings coupled in subtractive-dispersive mode. This pair acts as a tunable bandpass filter and passes a small spectral region of non-dispersed light to the final spectrograph stage. The final spectrograph has a 0.6 m length and is of asymmetrical Czerny-Turner design. For this work an 1800 gr/mm holographic grating was used, providing approximately 11 nm of spectral coverage at the detector plane.

All data acquisition was performed with a Dicam Pro intensified CCD camera. The sensor format is SuperVGA with a scan area of 8.6 mm (H) $\times$ 6.9 mm (V). This range is covered by 6.7 μm $\times$ 6.7 μm pixels, yielding sensor coverage of 1280 (H) $\times$ 1024 (V) pixels. The sensor is cooled by a two-stage Peltier thermoelectric cooler to an operating temperature of $-12\,^{\circ}$C in order to reduce the dark noise. The key element of an intensified CCD is the intensifier itself, which in addition to supplying gain to the signal can also be used to gate the intensifier. Gating the detector allows one to gather light only in a short window containing the laser pulse, greatly reducing the contribution of continuous background emission from the plasma.

Control of the camera was performed using a program called PCO Camware from the Cooke Corporation. This software suite allows detailed control over gating, gain, triggering, binning, and data output. The camera accepts a trigger input from the laser Q-switch via a BNC cable and then transmits the data from the camera to the computer via a fiber-optic cable. Due to the low density of the plasma investigated in this work and the poor quantum efficiency of the photocathode (only 10% at 532 nm), the pixels were binned into 8 (H) $\times$ 32 (V) super-pixels in order to improve the detection limit and reduce acquisition times.

III. Data Acquisition

The entire scattering system is controlled with a dedicated computer system that runs two programs, one that controls the camera and one that controls the laser system. Since the camera is gated to only detect signal in a small window containing the laser pulse the camera requires an accurate trigger pulse. For a sequence of laser shots the trigger is provided by a synchronized output on the laser control unit. The BNC trigger line is connected to the camera and provides a time-advanced rising edge trigger to the camera, which then waits a fixed delay before opening the electro-optical shutter on the camera. The camera shutter is only open for 20 ns each pulse, allowing the capture of the 6 ns (FWHM) laser pulse with some room for jitter in the electronics. For measurements with the laser off, the camera is triggered by an Agilent 33120A digital function generator operating at the laser repetition rate of 10 Hz. The shutter times are the same as for laser measurements so that the measured emission can be accurately subtracted from the total spectrum.

For all measurement conditions 27,000 acquisitions were taken, which was the limit determined by the memory available in the camera. Each individual acquisition is stored in a separate ascii file containing a two-dimensional matrix the size of the detector face, with each unit in the matrix corresponding to a binned super-pixel. The value of each matrix unit is the number of counts recorded during that acquisition.

IV. Measurement Procedure

A. Laser Measurements

Thomson scattering spectra are always determined by taking the difference of at least two separate measurements.[11] For this work two sets of laser data were taken at each thruster operating condition.

1. The first measurement is taken with the Hall-effect thruster operating at the nominal condition with the laser off. This data set contains the background emission spectrum of the thruster for that specific operating condition. Since the laser is off there is no stray light component. This will be referred to as the emission spectrum.

2. The second measurement is made with the thruster operating and the laser on. This measurement

contains the full spectrum, including Rayleigh scattering, Thomson scattering, the stray light, and the background plasma emission. This will be referred to as the total spectrum.

As a result of this process there are two data sets made up of 27,000 files each, with each file containing a single acquisition. These files are use to create a single corrected spectrum using a procedure detailed in a later section.

B. Probe Measurements

A double probe measurement was performed for each operating condition of the thruster after completion of the optical measurements. During the laser scattering and emission measurements the probe sits at a home position approximately 1.5 m downstream of the thruster and 0.5 m laterally off-axis from the thruster centerline. For probe measurements the motion table control software rapidly moves the probe into the measurement position such that the center of the double probe tips are centered in the scattering volume in the plasma (the laser is off at this time), and a single sweep is performed before moving back to the home position. The current and voltage during the sweep are recorded into an HDF5 file, along with all of the thruster operating parameters.

V. Data Processing

A. Double Probe

Probe data analysis was performed using the hyperbolic tangent method. The assumptions made for this analysis are as follows: the electron energy distribution in the plasma is Maxwellian, the probe is operating in the thin-sheath limit, and the probes are of equal area (the ion saturation currents are equal). When these conditions are satisfied the ideal I-V characteristic is a hyperbolic tangent curve given by:

$$I = I_{sat} \tanh\left(\frac{eV}{2k_B T_e}\right) \tag{1}$$

where I_{sat} is the ion saturation current, k_B is Boltzmann's constant, T_e is the electron temperature in Kelvin, and V is the voltage applied between the probes. A least-squares hyperbolic tangent fit was performed according to the following equation:

$$I(V) = A \cdot \tanh[B \cdot (V - C)] + D \cdot V + E \tag{2}$$

where A is the ion saturation current, B is proportional to the inverse of the electron temperature, D helps to compensate for sheath expansion in the saturation regions,[2] and C and E account for small offsets caused by stray capacitance in the probe system and gradients in the plasma.[12] An example of a double probe fit to actual data can be seen in Figure 1.

Calculation of electron temperature and density from a double probe trace is relatively simple. The electron temperature can be calculated directly through the following equation:

$$T_e = \frac{e}{2k_B B} \tag{3}$$

where T_e is in Kelvin. Calculation of plasma density is not as straight-forward. In order to calculate plasma density one needs to start with the ion saturation current. For a quasi-neutral Maxwellian plasma with $T_e = T_i$ the ion saturation current is given by:[13]

$$I_{sat} = \frac{1}{4} e n A_p v_{i,th} = e n A_p \sqrt{\frac{k_B T_i}{2\pi m_i}} \tag{4}$$

where e is the charge of an electron in Coulombs, n is the plasma density, A_p is the probe area, and $v_{i,th}$ is the ion thermal speed, and m_i is the ion mass. However, in Hall thruster plasmas $T_e \gg T_i$ and the ion saturation current is actually given by the Bohm ion current:[14]

$$I_{sat} = I_{Bohm} = 0.6 e n A_p \sqrt{\frac{k_B T_e}{m_i}} \tag{5}$$

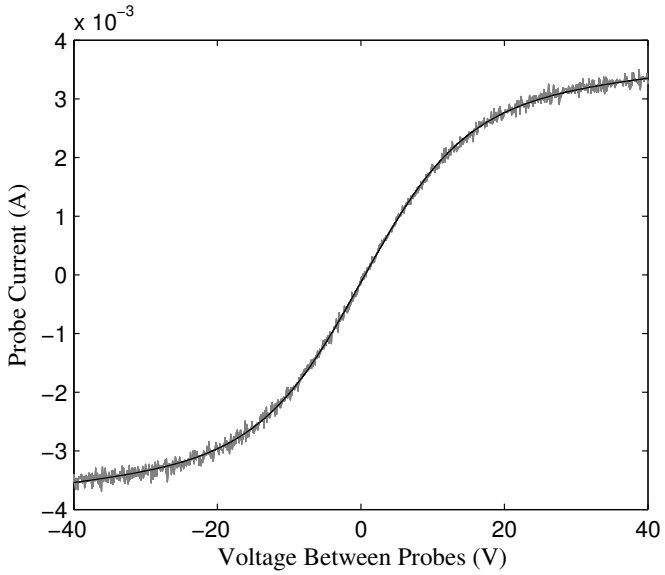

Figure 1. Actual double probe trace (gray) with curve fit (black).

This equation can then be arranged as follows to yield the plasma density:

$$n = \frac{I_{sat}}{0.6eA_p}\sqrt{\frac{m_i}{k_B T_e}} \tag{6}$$

B. Detector Noise Characteristics

Plasma conditions in the near-field plume of an HET produce a very small number of scattered photons that can be difficult to detect. When a photon arrives at the detector it impacts a photocathode and produces photoelectrons. These photoelectrons then enter a micro-channel plate (MCP) where they are amplified by secondary emission. After amplification the electrons impact a phosphor screen and are converted back into photons, which are then converted into counts by the CCD. Even if no photons arrive in an acquisition a count level is recorded due to various noise sources in camera. This noise is Gaussian with non-zero mean, and a histogram of this noise can be seen in Figure 2. Due to the amplification in the MCP, count levels generated by real photon arrivals will be larger than count levels generated purely by noise. Since most pixels do not receive any photons during a single exposure there is only noise recorded in most acquisitions, and if a series of acquisitions are simply averaged the scattered signal will be lost. When facing such a low scattered photon flux thresholding methods (such as photon counting) are typically implemented. The idea behind thresholding methods is that a count level is set and any count values below this level are considered to be non-events. If the count value exceeds the threshold it is considered that a photon arrival has occurred. Using this method it is possible to "build up" a spectrum over many acquisitions that should ideally only contain signal due to real photon detection events.

While this can be an effective way to separate real photon arrivals from non-events, thresholding methods do have one major drawback. Thresholding is a binary operation and if multiple-photons arrive in the same acquisition they are incorrectly recorded as a single photon. Most acquisitions contain no photons at all, and when Thomson photons do arrive at the detector there is typically only one (or on rare occasions more than one), and thresholding works fairly well. In contrast, Rayleigh calibration is performed at higher pressures and there are multiple photons arriving in every pulse. In these situations thresholding methods are somewhat ineffective, since underestimation of the Rayleigh signal can greatly affect the calculated density. In order to handle low photon flux and accurately record multiple photon arrivals a new data processing method was developed using a maximum likelihood estimation technique.

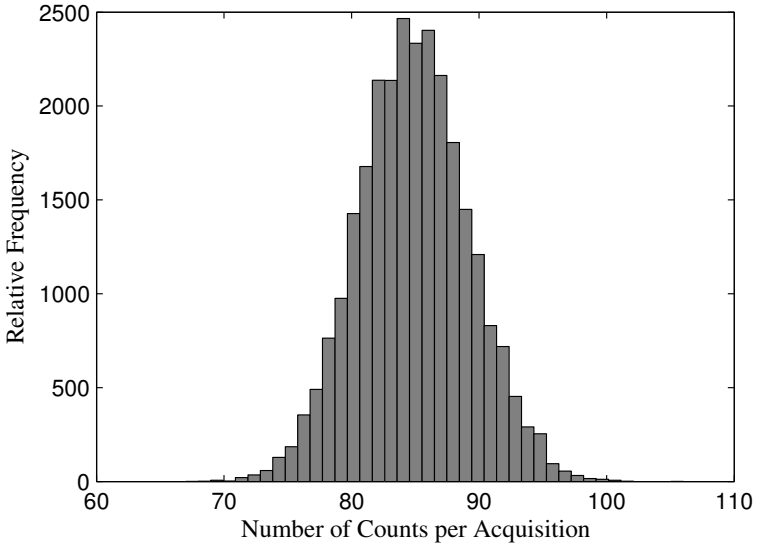

Figure 2. Histogram of the number of counts detected at a super-pixel with the spectrograph entrance slit closed over 27,000 acquisitions with an exposure time of 20 ns. These counts are purely due to noise and possess a mean of 85 counts and a standard deviation of 4.5 counts.

C. Maximum Likelihood Estimation

Maximum likelihood estimation is a technique that can be used to estimate the parameters of a distribution from a sample of data using knowledge of the probability density function for the system under investigation. To begin, one must specify the distribution whose parameters are the object of estimation. Let $x = \{x_1, x_2, \cdots x_n\}$ represent a set of random measurements from an unknown population. The probability density function that characterizes this unknown distribution can be written generically as $f(x|\mu)$, where the function f represents the probability of measuring the values in the vector x, given the fact that the distribution is known to be characterized by the parameter μ. Since the observations x_i are randomly obtained, they can be considered to be statistically independent, since measuring x_1 in no way affects future measurements. By definition, for a statistically independent random variable the probability of obtaining the measurements $x = \{x_1, x_2, \cdots x_n\}$ can be expressed as the product of the individual probabilities of each measurement,[15] given by:

$$f(x = \{x_1, x_2, \cdots x_n\}|\mu) = f_1(x_1|\mu) \cdot f_2(x_2|\mu) \cdots f_n(x_n|\mu) \tag{7}$$

where μ can take on any value that satisfies the distribution f.

This statement is predictive in nature, in that it is assumed that if the form of f and its characteristic parameter μ is known, predictions can be made concerning measurements of this distribution. In reality, the problem is reversed in practical statistics. One does not usually know the exact parameters of a distribution, such as the average height of an American boy between the ages of 8 and 12, but it is often the case that a researcher has thousands of actual measurements of boys in this age range. The researcher wants to know what the average height of the entire population of 8 – 12 year old boys in America is, and she or he only has a small measurement sample from which an estimation of this parameter can be made. Attempts to determine this parameter from a given sample of heights can be thought of as an inverse problem, and this is the domain of the concept of "likelihood".

In order to determine the solution to this inverse problem, the likelihood function can be defined by reversing the roles of the data and the distribution parameters,[15] yielding:

$$L(\mu|x) = f(x|\mu) = \prod_{i=1}^{n} f(x_i|\mu) \tag{8}$$

In this case the measurements, x, are considered to be fixed and the value of μ is varied while computing

the value of L. The value of μ that maximizes this function is the maximum likelihood estimator of μ, often written as $\hat{\mu}$.

Maximizing the likelihood function can be computationally difficult. For large samples calculating the likelihood for each estimate of the characteristic parameters can be time-consuming. Another problem that often occurs is that when computing the maximum likelihood as written in equation 8, one may end up with many very large or very small numbers that must be multiplied. Computers have difficulty handling very large and very small numbers, and the natural logarithm of the likelihood function is often maximized instead. In this case the convention is to refer to this new function as the log-likelihood, given by:

$$\ln\left[L(\mu|x)\right] \tag{9}$$

Since the logarithm is a monotone transform, the resulting value of the maximum likelihood estimator is the same whether the likelihood or log-likelihood function is maximized.

D. MLE Applied to Laser Thomson Scattering

Maximum likelihood estimation requires a statistical model of the system to which it is being applied. Scattering events are random occurrences that happen sparsely in time and very few photons arrive at a single super-pixel, even over tens of thousands of acquisitions. Such events are well modelled by the Poisson distribution, given by:[16]

$$P(X = x) = \frac{e^{-\mu}\mu^x}{x!} \tag{10}$$

where X is the random variable and μ is the characteristic parameter of the distribution. By convention, $0^0 = 1$ and $0! = 1$. For Poisson processes μ is both the mean and the variance of the distribution.

Since there are so few photon arrivals, most acquisitions contain only read noise with a normal distribution centered on the mean value of the noise, μ_N (in counts), for that super-pixel. When a photon does arrive at the detector it will produce a count value given by $\mu_N + k\beta$, where k is the number of photons arriving during the acquisition time and β is the mean camera gain in counts per photon. There will be some small variation in the count level produced by any given photon due to noise present in the amplification process and noise from sources in the camera (dark noise, read noise, etc.). A sample histogram demonstrating this distribution of counts can be seen in Figure 3.

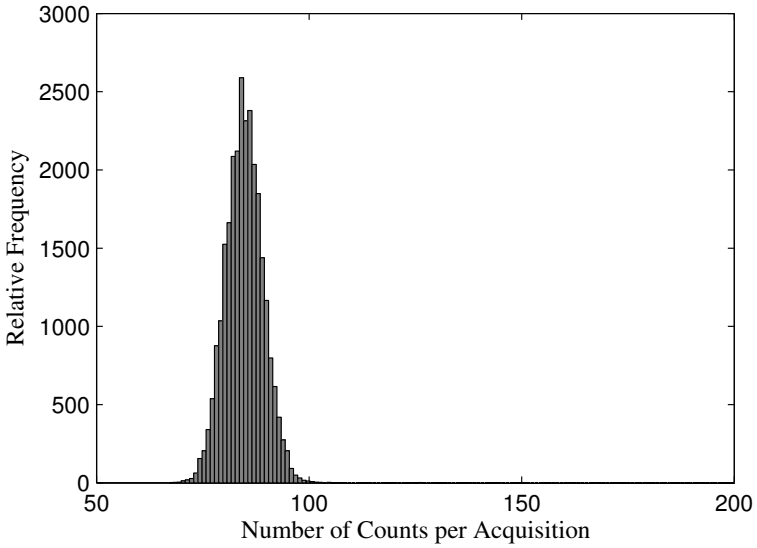

Figure 3. Histogram of the number of counts detected at a super-pixel during emission spectrum acquisition with an exposure time of 20 ns. This figure demonstrates that most acquisitions contain only read noise centered on the mean of the noise μ_N.

Using knowledge of the noise parameters for the system and the nature of photon arrival the data can be processed in a way that essentially performs advanced photon counting, where multiple photon arrivals

are counted accurately. First, the distribution is shifted by subtracting μ_N from the count values such that the mean of the count values produced by non-events is zero. Second, all values are divided by the detector gain, β, with the goal of transforming the data from counts into the number of photons that produced that count value. A sample histogram of the data after these operations have been performed can be seen in Figure 4. Because there is noise from various sources present in the data the values do not round exactly to integer values (e.g. it appears as if fractional photons are arriving). However, the variance of the noise is such that 4 standard deviations is less the $\beta/2$, which means that 99.994% of the time noise will not cause a count value generated by k photons to appear to have been generated by $k \pm 1$ photons. Knowing this, the data can be rounded to the nearest integer value with confidence that this is the number of photons that produced that count level. The result of this operation can be seen in Figure 5.

When the data are processed in this manner the resulting histogram is very similar to a Poisson distribution (described previously) with a very small characteristic parameter μ that corresponds to the mean photon arrival rate. If one were to generate a Poisson random variable to simulate photon arrivals with $\mu \ll 1$ and sample it 27,000 times, the result would be mostly zeros corresponding to non-events and very few arrivals corresponding to one or more photons. The transformed data follow this distribution reasonably well and can be fit using a maximum likelihood estimation algorithm with a Poisson model. The resulting maximum likelihood estimator, $\hat{\mu}$, provides the most likely arrival rate for the given data, which includes multiple photon events. For the processed data shown in Figure 5 the calculated value of $\hat{\mu}$ is 0.0014 photons per acquisition.

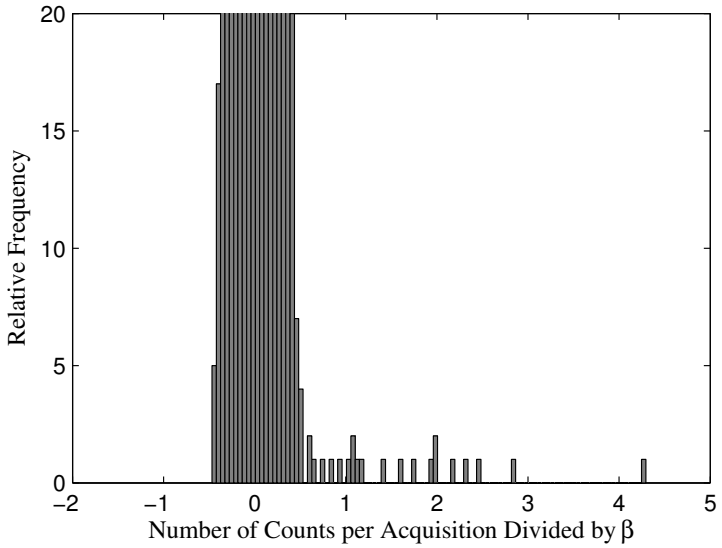

Figure 4. Histogram of emission data after being shifted by μ_N and divided by β.

VI. MLE Processing Algorithm

Processing of the laser Thomson scattering data is performed using a multi-step algorithm. As described in Section III, the iCCD program stores each individual acquisition as a separate ascii file. Prior to performing plasma measurements, noise measurements are performed with the spectrograph entrance slit closed. Using these measurements the mean (μ_N) and standard deviation (σ_N) of the noise are calculated for each individual super-pixel and are stored in new variables. The noise across the detector is not uniform, and the noise parameters are used to perform non-uniformity compensation.

Each acquisition for the plasma measurements and the Rayleigh calibration measurements are also stored in individual ascii files. These files are loaded into Matlab® where they are combined into 3-D matrices containing all of the individual acquisitions. After this pre-processing step there are three matrices containing the total spectrum measurements, the emission spectrum measurements, and the Rayleigh spectrum measurements (for calibration purposes, described later).

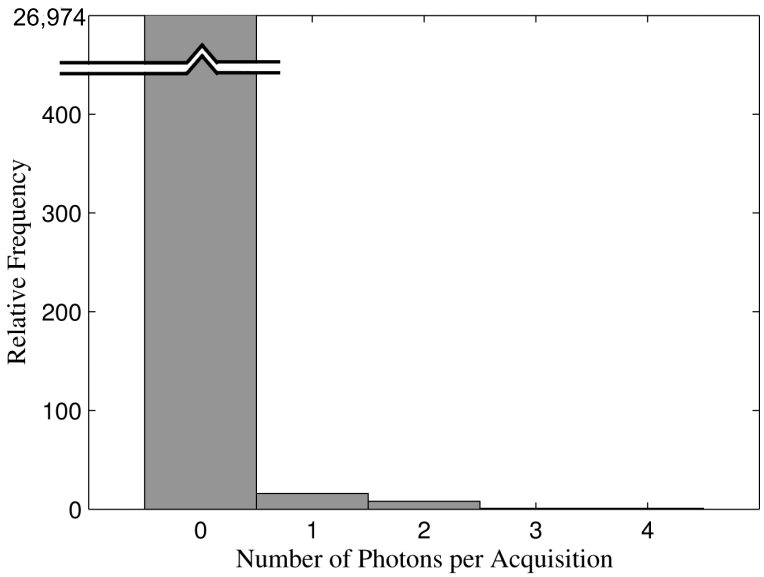

Figure 5. Histogram of fully processed emission data, zoomed in to clearly display the non-zero bins. The value of $\hat{\mu}$ determined by maximum likelihood estimation is 0.0014.

The algorithm used to process the data is as follows:

1. A single super-pixel is selected and a vector containing the count values for all acquisitions is created from the master data matrix.
2. The mean value of the noise at this super-pixel, μ_N as determined from the pre-recorded noise measurements, is then subtracted from all of the values in order to shift the noise to zero mean.
3. After shifting, all values are divided by the mean detector gain β.
4. All values are then rounded to the nearest integer, which combined with the previous step converts the data from counts to photons.
5. This corrected vector is provided to Matlab's® maximum likelihood estimation function and fit with a Poisson distribution. The maximum likelihood estimator, $\hat{\mu}$, corresponds to the mean photon arrival rate at that super-pixel.

This process was performed on every super-pixel two times, once for each of the spectra sequences measured (total and emission). The results of this process are two-dimensional matrices the size of the binned detector that contain the estimated photon arrival for each data set. The corrected spectrum is constructed by simply subtracting the emission spectrum from the total spectrum and applying a mask in software to the stray/Rayleigh component near the laser wavelength.

Normally a stray light measurement is performed with the laser on and the discharge off, and this spectrum is also subtracted from the total spectrum to create the final corrected Thomson spectrum. A set of stray light measurements was performed at the beginning of this test before the thruster was turned on, and since the stray light does not depend on the discharge conditions, additional measurements were not performed at each operating condition. After the test it was discovered that a coating was deposited on the lens during thruster operation, and since the coating was not present during the initial stray light measurements, the unattenuated stray light spectrum could not be subtracted from the attenuated total spectrum.

By not subtracting the stray light contribution it is possible that the spectral shape and amplitude were affected. The triple spectrograph has excellent stray light redistribution of 8×10^{-5} at $\Delta\lambda = 1$ nm from the laser wavelength, and decreases rapidly to $\approx 5 \times 10^{-6}$ for $\Delta\lambda > 3$ nm. This stray light redistribution level is very low, but without having measurements of the stray light it is possible that

the LTS measurements performed in this work will overestimate the electron density and also modify the calculated electron temperature. Further investigation of how this lack of stray light subtraction affects the scattered spectrum is currently in progress.

1. *Determination of Electron Temperature and Density*

Although in principle no assumptions are needed regarding the electron distribution function, the low photon arrival rate present in this experiment yields a low signal-to-noise ratio (SNR). Small deviations from a Maxwellian distribution are difficult to detect in this case, and without high SNR measurements indicating otherwise a Maxwellian distribution was assumed. Using this assumption a Gaussian fit can be performed and the conventional thermal temperature can be used to characterize the distribution. A non-linear least-squares Gaussian fit was performed on the corrected scattering spectrum and the value of σ determined from the fit was used to calculate the $1/e$ width according to the following equation:

$$\Delta\lambda_{1/e} = \sqrt{2\sigma^2}. \tag{11}$$

This value was then substituted into the following equation for the electron temperature:[11]

$$T_e = \frac{m_e c^2}{8k_B \sin^2(\theta/2)} \cdot \left(\frac{\Delta\lambda_{1/e}}{\lambda_i}\right)^2 \tag{12}$$

which can also be expressed (for our particular dispersion and binning) as:

$$T_e = 0.00905 \cdot \sigma^2 \tag{13}$$

where T_e is in eV and σ is in super-pixels. An example of a corrected spectrum and corresponding fit can be see in Figure 6.

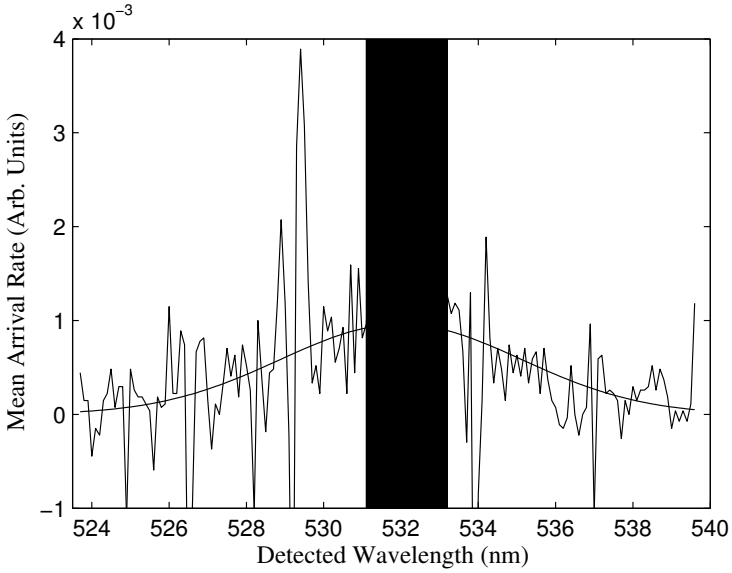

Figure 6. Corrected Thomson scattering spectrum as determined using the maximum likelihood estimation technique. $T_e = 8.9\,eV$, $n_e = 7.2 \times 10^{17}\,m^{-3}$.

An absolute measurement of density can be obtained by performing Rayleigh calibration on a gas of known pressure.[17] The density is determined according to the following equation:[18]

$$n_e = n_R \frac{\sigma_R}{\sigma_T} \frac{P_T}{P_R} \frac{\int_\lambda I_T}{\int_\lambda I_R}. \tag{14}$$

where n_R is the number density of the calibration gas (for this work N_2 was used), $\frac{P_T}{P_R}$ is the ratio of laser powers for the two measurements, and $\int_\lambda I_x$ is the integrated intensity of each spectrum. The cross-sections for Thomson and Rayleigh scattering are known constants and the number density during Rayleigh

calibration can be calculated using the ideal gas law. The integral of the Rayleigh spectrum is performed numerically, and for the Thomson spectrum the integral is calculated from the amplitude and standard deviation of the fit to the corrected spectrum.

Rayleigh calibration was performed prior to pumping down the vacuum chamber to hard vacuum. The chamber was roughed down to 2.5 Torr and the left overnight to allow dust to settle. The laser was then fired into the vacuum chamber and the camera recorded the scattered light with the same settings that were used for laser measurements (27,000 acquisitions, 20 ns exposure). After obtaining the Rayleigh calibration data the chamber was pumped down to hard vacuum overnight and plasma measurements were performed over the next few days.

VII. Results and Discussion

Both laser and probe measurements of temperature and density were performed at a variety of operating conditions. At a given value of discharge voltage and mass flow rate the magnet current was adjusted to minimize the discharge current. The discharge voltage/mass flow rate test matrix was pseudo-randomized to avoid systematic errors. All of the operating conditions (with the order of measurement) can be seen in Table 1. For all thruster operating conditions the cathode was operated at a mass flow rate of 5 SCCM of xenon, with 0.5 A of current drawn by the keeper. The discharge current at each operating condition and the magnet current can be seen in Tables 2 and 3, respectively. The measured pressure in the vacuum chamber during each measurement can be seen in Table 4.

Table 1. Test Matrix with Measurement Order

Mass Flow (SCCM)	Discharge Voltage (V)				
–	250	300	350	400	450
40	–	1	6	4	–
50	–	5	3	8	–
60	13	9	2	7	11
70	–	–	12	–	–
80	–	–	10	–	–

Table 2. Discharge current (A) for each operating condition.

Mass Flow (SCCM)	Discharge Voltage (V)				
–	250	300	350	400	450
40	–	3.40	3.34	3.34	–
50	–	4.40	4.30	4.24	–
60	5.30	5.27	5.30	5.20	5.27
70	–	–	6.25	–	–
80	–	–	7.40	–	–

A. Temperature

The first set of results that will be presented are the double probe measurements, since electrostatic probes are the accepted method of measuring plasma temperature and density in Hall-effect thruster plasmas. Measured electron temperature for each operating condition can be seen in Table 5. The electron temperature in the near-field plume varied little with discharge conditions. Electron temperature was not expected to exhibit dependence on the mass flow rate, but it was somewhat surprising to see that the discharge voltage had minimal effect on the measured electron temperature. Some dependence on discharge voltage was expected based on fast-probe measurements of a Hall thruster performed by Raitses et. al.[3] The geometry of the

Table 3. Magnet current (A) for each operating condition.

Mass Flow (SCCM)	Discharge Voltage (V)				
–	250	300	350	400	450
40	–	3.00	3.00	3.00	–
50	–	3.25	3.25	3.25	–
60	3.00	3.00	3.75	4.00	5.00
70	–	–	4.50	–	–
80	–	–	5.00	–	–

Table 4. Background pressure ($\times 10^{-5}$ Torr) for each operating condition.

Mass Flow (SCCM)	Discharge Voltage (V)				
–	250	300	350	400	450
40	–	1.60	3.30	1.70	–
50	–	7.30	2.00	2.00	–
60	2.40	2.80	2.20	2.50	2.20
70	–	–	2.50	–	–
80	–	–	2.90	–	–

thruster used in this study was different than the thruster used by Raitses, but the general trend of electron temperature increasing with discharge voltage was expected.

Table 5. Electron temperature in eV as measured by electrostatic double probe.

Mass Flow (SCCM)	Discharge Voltage (V)				
–	250	300	350	400	450
40	–	8.7	8.2	7.9	–
50	–	7.6	7.8	10	–
60	8.6	8.3	7.1	9.4	7.0
70	–	–	8.2	–	–
80	–	–	7.1	–	–

Calculated electron temperature determined from the LTS data for each operating condition can be seen in Table 6. At lower discharge voltages and mass flow rates the values from both measurement methods agree fairly well, but at increased mass flow rates and discharge voltages the LTS values are significantly higher than the values determined from the probe measurements. The temperature estimates increase at higher voltages, which was expected but not seen in the double probe data. Electron temperature also rises at the higher mass flow rates, which was not expected.

A comparison of electron temperature versus mass flow rate at a discharge voltage of 350 V can be seen in Figure 7. The probe data produced nearly constant electron temperature across all mass flow rates, which was the expected behavior. The LTS data produced a very different trend, with a large rise in electron temperature at the higher mass flow rates. Using the probe values as a reference the LTS data produced temperature estimates that were low below 60 SCCM and high above, with variations ranging from as little as 1.3 percent at 50 SCCM to as much as 225 percent at 80 SCCM.

A comparison of electron temperature versus discharge voltage for a fixed mass flow rate of 60 SCCM can be seen in Figure 8. The LTS values show a clear increase in electron temperature with discharge voltage, whereas the probe values do not. This indicates that one of the measurements is unreliable. The laser data

Table 6. Electron temperature in eV as determined from the LTS data.

Mass Flow (SCCM)	Discharge Voltage (V)				
–	250	300	350	400	450
40	–	5.6	4.9	8.1	–
50	–	8.3	7.9	20	–
60	1.4	1.2	3.4	21	38
70	–	–	14	–	–
80	–	–	23	–	–

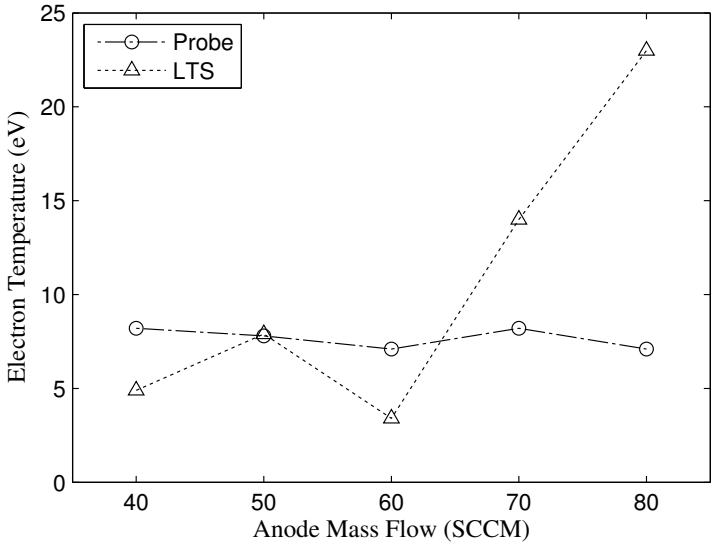

Figure 7. Comparison of electron temperature measurements vs. mass flow rate at a fixed discharge voltage of 350 V.

at higher voltages may be faulty due to some unknown reason, such as poor optical alignment induced by thermal effects on the system. It is also possible that the presence of the probe somehow cools the plasma (for example through ablation) and affects the measured temperature. The low SNR of the LTS measurements makes it difficult to confirm which method produced incorrect temperature estimates.

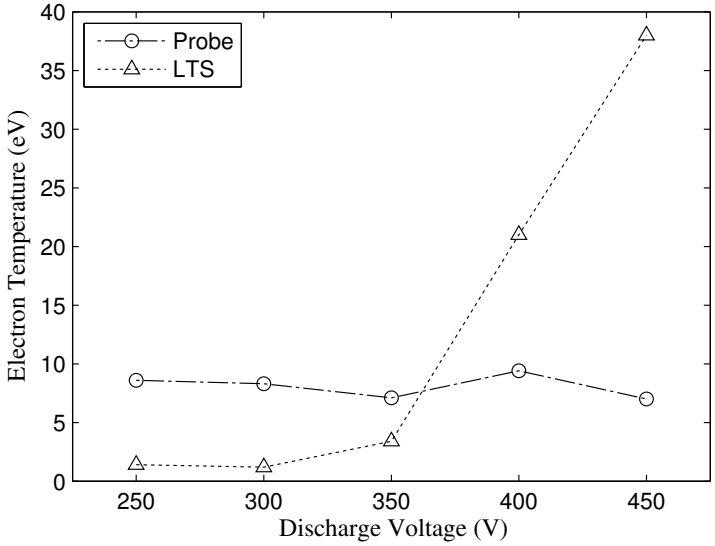

Figure 8. Comparison of electron temperature measurements vs. discharge voltage at a fixed mass flow rate of 60 SCCM.

B. Density

Plasma density calculated from the double probe measurements can be seen in Table 7. Density ranged from approximately $8 \times 10^{17}\, m^{-3}$ to $1.3 \times 10^{18}\, m^{-3}$. Like the electron temperature, the plasma density measurement matrix is rather flat and does not exhibit any clear trends. It was expected that the plasma density at the measurement point would increase with increased mass flow rate, but this trend was not seen.

Table 7. Electron number density ($\times 10^{18}\, m^{-3}$) as measured by electrostatic double probe.

Mass Flow (SCCM)	Discharge Voltage (V)				
–	250	300	350	400	450
40	–	0.8	1.3	1.0	–
50	–	0.9	0.9	1.0	–
60	1.0	1.3	0.8	1.3	0.8
70	–	–	1.2	–	–
80	–	–	0.9	–	–

The plasma density determined from the LTS data for each operating condition can be seen in Table 8. Plasma density ranged from approximately $1 \times 10^{17}\, m^{-3}$ to $7 \times 10^{17}\, m^{-3}$. There does not appear to be any clear correlation between plasma density and mass flow rate or discharge voltage.

A comparison of the plasma density versus mass flow rate at a fixed discharge voltage of 350 V can be seen in Figure 9. Unlike the temperature measurements, the plasma density measurements derived from probe data and LTS data have a similar character. For both methods there is little variation in the density and no clear trends with respect to discharge voltage and mass flow rate. In general, the LTS estimates are lower than the double probe estimates by 30 - 100 percent, but closer to the expected density in the near-field plume.[2]

Table 8. Electron number density ($\times 10^{17}\, m^{-3}$) as determined from the LTS data.

Mass Flow (SCCM)	Discharge Voltage (V)				
–	250	300	350	400	450
40	–	7.1	3.8	4.0	–
50	–	5.6	4.0	3.4	–
60	1.0	3.3	3.7	5.1	4.3
70	–	–	2.4	–	–
80	–	–	6.2	–	–

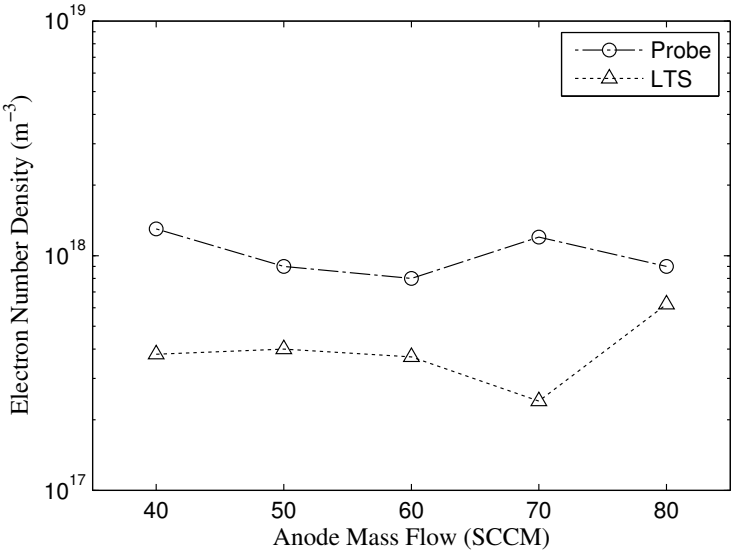

Figure 9. Comparison of plasma number density measurements vs. mass flow rate at a fixed discharge voltage of 350 V.

A comparison of the plasma density versus discharge voltage for a fixed mass flow rate of 60 SCCM can be seen in Figure 10. The probe values are flat across all discharge voltages, but the LTS values display a slight rise with increasing discharge voltage. If the electron temperature is in fact elevated at higher discharge voltages the ionization rate would increase, leading to an increase in density.

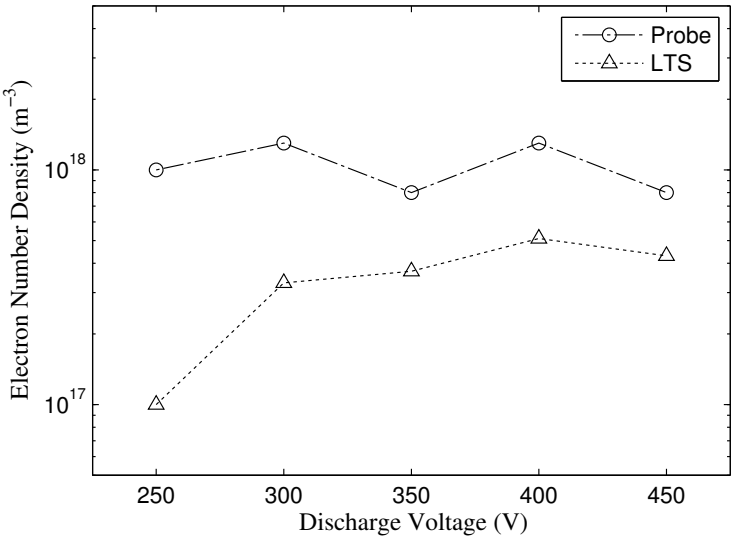

Figure 10. Comparison of plasma number density measurements vs. discharge voltage at a fixed mass flow rate of 60 SCCM.

VIII. Conclusion

This study has demonstrated that it is possible to perform laser Thomson scattering measurements of electron temperature and density in the near-field plume of a Hall-effect thruster. Doing so required use of high-performance equipment along with development of a new method of processing the scattered signal. The laser data processed with the MLE method produced reasonable values of temperature and density, but agreement with probe measurements was not strong. Although this could be interpreted to mean that the probe measurements have been compromised by the disturbance to the plasma, the low SNR of the laser data does not yet justify this claim and further work is required. In theory, Thomson scattering should provide the greatest accuracy for electron temperature measurements, since the electron velocity distribution is being measured directly. In practice, the low plasma density in the plume produces low SNR measurements of the scattered spectrum, and there is significant uncertainty in the determination of electron temperature and density (especially without accurate stray light measurements). Improvements in system performance will increase the certainty in the laser measurements and provide more accurate measurements of electron temperature and density in the near-field plume.

References

[1]Gascon, N. M., Dudek, M., and Barral, S., "Wall Material Effects in Stationary Plasma Thrusters. I. Parametric Studies of an SPT-100," *Phys. Plasmas*, Vol. 12, No. 10, 2003, pp. 4123–4136.

[2]Haas, J., *Low-Perturbation Interrogation of the Internal and Near-Field Plasma Structure of a Hall Thruster Using a High-Speed Probe Positioning System*, Ph.D. thesis, University of Michigan, 2001.

[3]Raitses, Y., Staack, D., Dorf, L., and Fisch, N. J., "Experimental Study of Acceleration Region in a 2 kW Hall Thruster," *39th AIAA/ASME/SAE/ASEE Joint Propulsion Conference & Exhibit*, Huntsville, AL, 2003.

[4]Ross, J. L., *Probe Studies of a Hall Thruster at Low Voltages*, Ph.D. thesis, Michigan Technological University, 2011.

[5]Maiman, T. H., "Stimulated Optical Emission in Ruby," *Nature*, Vol. 187, 1960, pp. 493–494.

[6]King, D., "Development of the BPT Family of U.S.-Designed Hall Current Thrusters for Commercial LEO and GEO Applications," *34th AIAA/ASME/SAE/ASEE Joint Propulsion Conference & Exhibit*, Cleveland, OH, 1998.

[7]Wilson, F., "Development Status of the BPT Family of Hall Current Thrusters," *35th AIAA/ASME/SAE/ASEE Joint Propulsion Conference & Exhibit*, Los Angeles, CA, 1999.

[8]de Grys, K., "BPT Hall Thruster Plume Characterization," *35th AIAA/ASME/SAE/ASEE Joint Propulsion Conference & Exhibit*, Los Angeles, CA, 1999.

[9]Kieckhafer, A. W., Massey, D. R., King, L. B., and Sommerville, J. D., "Effect of Segmented Anodes on the Beam Profile of a Hall Thruster," *40th AIAA/ASME/SAE/ASEE Joint Propulsion Conference & Exhibit*, Fort Lauderdale, FL, 2004.

[10]Sommerville, J. D. and King, L. B., "Effect of Cathode Position on Hall-Effect Thruster Performance and Cathode Coupling Voltage," *43rd AIAA/ASME/SAE/ASEE Joint Propulsion Conference & Exhibit*, Cincinnati, OH, 2007.

[11]van de Sanden, M. C. M., *Laser Scattering on Low Temperature Plasmas*, Doctoral dissertation, Eindhoven University of Technology, 2002.

[12]Sommerville, J. D., *Hall-Effect Thruster-Cathode Coupling*, Dissertation, Michigan Technological University, 2009.

[13]Hutchinson, I. H., *Principles of Plasma Diagnostics*, Cambridge University Press, New York City, 2nd ed., 2002.

[14]Merlino, R. L., "Understanding Langmuir Probe Current-Voltage Characteristics," *Am. J. Phys.*, Vol. 75, No. 12, 2007, pp. 1078–1085.

[15]Myung, J., "Tutorial on Maximum Likelihood Estimation," *Journal of Mathematical Psychology*, Vol. 47, 2003, pp. 90–100.

[16]Yates, R. D. and Goodman, D. J., *Probability and Stochastic Processes*, John Wiley & Sons, Inc., Hoboken, 2nd ed., 2005.

[17]Muraoka, K., Uchino, K., and Bowden, M. D., "Diagnostics of Low-Density Glow Discharge Plasmas Using Thomson Scattering," *Plasma Phys. Control. Fusion*, Vol. 40, 1998, pp. 1221–1239.

[18]Kunze, H.-J., *The Laser as a Tool for Plasma Diagnostics*, Plasma Diagnostics, North-Holland Publishing Company, Amsterdam, 1968.